Optical scanning of a laser triangulation sensor for 3D imaging

Johannes Schlarp, Ernst Csencsics, and Georg Schitter, *Senior Member, IEEE,*

Abstract—In scan-based 3D systems the achievable measurement time is strongly restrained by the moving mass. This limitation can be relaxed, by scanning the optical path instead of moving the entire sensor, such that a higher measurement speed can be achieved. This work deals with the design, control and the measurement results of a scanning triangulation sensor in which the illumination and reflection paths of the sensor are scanned by a fast steering mirror (FSM). The system architecture is determined using ray-tracing simulations, such that the performance of the scanning system can be determined in advance. To scan the area of interest with the FSM, conventional raster trajectories as well as Lissajous trajectories are employed, which provide an early overview of the scan area. For tracking these trajectories, PID and dual tone controllers are used, respectively. Experimental results demonstrate that for both scan trajectories the sample can be captured correctly, with a framerate of one frame per second, a maximum spatial resolution of 130 μm and a field of view of 11.5x18.5 mm.

Index Terms—3D sensor, laser sensor, system analysis and design, scan trajectories

I. Introduction

To meet the increasing quality requirements in production processes, high-resolution three-dimensional measurement systems are required [1]–[5]. Many of these systems are based on optical measurement principles, as in addition to the high resolution, a high measurement speed can be achieved [6], [7]. Optical measurement systems are available as point sensors, line sensors or 3D scanners. The measurement range of 3D scanners can reach from a few millimeter for structured light sensors, up to several hundred meters for time of flight based sensors [8]. The achievable resolution is, however, limited to several millimeters for a time of flight sensor [9] and $10\mu m$ for structured light sensors [10]. Point and line sensors can overcome this limitation and achieve resolutions up to a few nanometre [11]. To generate a three-dimensional image with an optical point or a line sensor, they are frequently combined with external actuators, like coordinate measurement machines [12] or linear stages [13] to enable a scanning motion [2]. In such mechanical scanning systems the location of the sample, sensor (Fig. 1(a)), or even both is varied [14]. Therefore, the achievable measurement time is strongly determined by the actuation force and thus the positioning bandwidth of the actuators. Manipulating only the optical path (Fig. 1(b)) of the optical sensor can resolve this limitation, since the moving mass of such an optical scanning system

The authors are with the Christian Doppler Laboratory for Precision Engineering for Automated In-Line Metrology at the Automation and Control Institute, Technische Universität Wien, A-1040 Vienna, Austria. Corresponding author email: schlarp@acin.tuwien.ac.at

is smaller as compared to a classical mechanical scanning system, which leads to a lower measurement time [15], [16]. Additionally, the optical scanning system forms a compact unit, such that a simplified integration in the measurement application can be realized [16]. Such optical scanning systems have already been developed for confocal sensors [17] and laser line sensors [16].
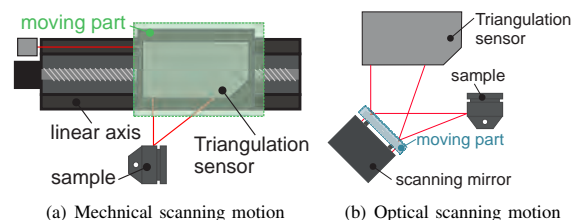

Fig. 1. Schematic setups of scanning sensor systems. (a) shows a conventional system, which varies the position of the sensor. (b) depicts an optical scanning system, in which the optical path of the sensor is manipulated by a scanning mirror.

Due to their large measurement range as well as their high resolution, laser triangulation sensors are one of the most commonly used optical sensors in dimensional metrology and quality control tasks [18]. The sensor projects a collimated light beam on the sample [10], [19]. At the point where the beam irradiates the sample, light is scattered. This scattered light is imaged onto the detector, by means of a lens. With the measured lateral position of the projected point on the detector and the geometry of the sensor the distance between the sensor and the sample can be determined [20].

Most often rotating polygons or galvanometers are used as scanners in optical scanning systems [16], [21]. The drawbacks of these systems are the large rotational inertia and the poor linearity during fast linear scanning [22]. MEMS scanners achieve high resonance frequencies as well as large actuation ranges, but their application in scanning systems is limited due to the small aperture size [23]. Fast steering mirrors (FSMs) feature a small rotational inertia as well as a fast response time [22]. Due to their compressed design, it is additionally possible to integrate them into compact scanning systems [16], [24]. They are driven by either electromagnetic [25], [26] or piezoelectric actuators [27], resulting in a large actuation range or a larger bandwidth, respectively. To scan the laser spot over the area of interest scan trajectories are required. Raster and Lissajous-based scan trajectories are commonly employed in scanning systems, like scanning probe microscopy (SPM) [28], [29], scanning tunnelling microscopy (STM) [30], or atomic

force microscopes (AFMs) [31].

The contribution of this paper is the design, the integration and the control of an optical scanning triangulation sensor system, which achieves a high image quality with a low moving mass. The system architecture and the geometrical relations of the scanning laser triangulation sensor are derived in Section II. The experimental setup and the implemented scan trajectories are shown in Section III. To track the desired trajectories, feedback position controllers are designed in Section IV. The measurement results are validated in Section V and Section VI concludes the paper.

II. SYSTEM DESIGN

A. Simulation

Potential system architectures of the optical scanning system can be evaluated in advance by using ray-tracing simulations. This enables a quick and easy comparison of the crucial parameters of the system, like the achievable lateral scan range or aberrations and errors due to misalignment. For the simulation the properties and positions of all optical components are set in advance. Based on these specifications, the ray-tracing simulation software (Matlab, Mathworks, Natick, USA) calculates and depicts the resulting ray path.

The scanning system should achieve a lateral scan range in the tenths of millimeter range. Since FSMs achieve a angular range in the single digit range, the sample must be sufficiently far away from the sensor to obtain the selected scan area, such that a sensor with a measurement range of 100 mm is selected. The laser triangulation sensor (Type: ILD 2300-100, Micro-Epsilon GmbH, Germany) forms the base for the system architecture. To observe the diffusely scattered point over the entire lateral scan range, the illumination and reflection path are manipulated by the FSM. Since the wavelength of the laser beam is large compared to the roughness of the mirror surface, the basic measurement geometry from the perspective of the triangulation sensor is not affected. As a result, the system architecture satisfies the Scheimpflug condition, leading to a sharp projection of the diffusely scattered point from the sample onto the detector at every point of the scan area [20]. Fig. 2 shows the results of the ray-tracing simulation for the optical scanning system for different lateral positions. The position of the laser spot on the sample is manipulated along the y or x-axis, by tilting the mirror surface around the x or yz'-axis, respectively. Commercial FSMs are mostly available with round or slightly elliptical mirrors of a specific diameter, e.g. one inch, two inches. To maintain the basic measurement geometry of the sensor, both optical paths need to be manipulated by the same mirror. The distance between sensor and FSM strongly affects the achievable lateral scan range of the scanning system [16]. In order to manipulated both optical paths close to the sensor, a mirror with an aperture size of two inches (Type: OIM102, Optics In Motion LLC, Long Beach, USA) is used. The lateral scan range is maximized, if the mirror is placed parallel to the yz' plane, which is tilted by $45°$ with respect to the z-plane.

B. Geometric relations for data reconstruction

In conventional mechanical scanning point sensor systems, the position of the sample or sensor is manipulated by external position controlled actuators. Thereby, the surface profile of the sample, described by the absolute values x_s, y_s and z_s, can be directly reconstructed, from the position of the actuators and the measured distance. In the proposed optical scanning system the measured variables include the value z_{meas} which is acquired by the triangulation sensor and the angular positions $\Delta\alpha$ and $\Delta\beta$ of the FSM. Since the surface profile cannot be directly obtained from these quantities, the geometric relations to calculate the absolute values from the measured quantities need to be evaluated [16].
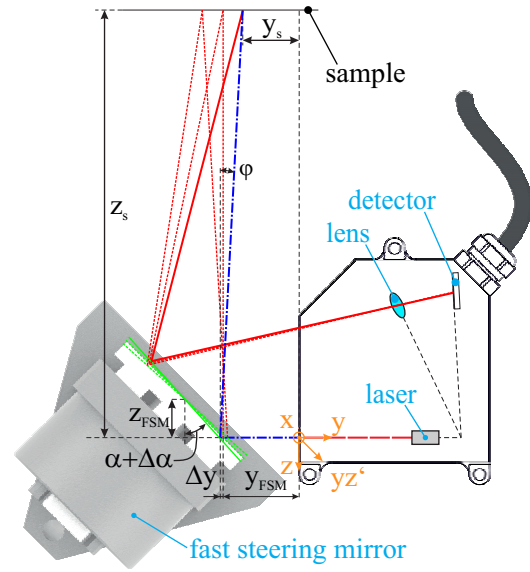

Fig. 2. Illustration scheme for ray tracing process in the triangulation sensor.

The determination of these relations is based on the schematic shown in Fig. 2. Since the laser beam emitted from the sensor does not hit the center of the FSM, an additional translational shift in the y-direction occurs [16]. This lateral displacement Δy, shown in Fig. 2, can be calculated by

$$\Delta y = z_{FSM}[\tan(\alpha) - \tan(\alpha - \Delta\alpha)], \quad (1)$$

with z_{FMS} the position in z-direction and α the orientation of the FSM. To calculate the absolute values, the two angles φ and ϑ of the laser beam reflected from the FSM are required. The angle φ is located in the yz plane (shown in Fig. 2), while the angle ϑ is located in the xz plane. By using the law of reflection [20], the two angles can be calculated to

$$\varphi = 90° - 2\alpha - 2\Delta\alpha \quad (2a)$$

$$\vartheta = (2\Delta\beta) \cdot \cos(\alpha + \Delta\alpha), \quad (2b)$$

in which $\Delta\alpha$ and $\Delta\beta$ represent the deviations from the initial angular position of the mirror around the x and yz'

axis (shown in Fig. 2). With trigonometric functions the geometrical relations for the scanning laser triangulation system can be derived to

$$x_s = [z_{meas} - y_{FSM} - \Delta y] \cos(\varphi) \sin(\vartheta) \quad \text{(3a)}$$
$$y_s = [z_{meas} - y_{FSM} - \Delta y] \sin(\varphi) \cos(\vartheta) \quad \text{(3b)}$$
$$\quad - y_{FSM} - \Delta y$$
$$z_s = - [z_{meas} - y_{FSM} - \Delta y] \cos(\varphi) \cos(\vartheta), \quad \text{(3c)}$$

with y_{FSM} the position of the FSM in y-direction and z_{meas} the distance measured by the sensor (blue dash-dotted line). To avoid a collision between FSM and sensor the distances y_{FSM} and z_{FSM}, depicted in Fig. 2, are set to 10 mm and 16.5 mm, respectively. As described earlier, the lateral scan range is maximized, if the orientation of the mirror around the x-axis α is 45°. The field of view of the measurement system is 4.3x8 mm at the minimum distance z_s of 60 mm and expands to 11.5x18.5 mm towards the lower end of the measurement range of 158.8 mm.

III. System hardware and scan trajectories

A. Experimental setup

Fig. 3 shows the experimental setup of the scanning laser triangulation sensor. As can be observed, the laser sensor and the FSM form a compact unit, such that the system can be easily integrated in the measurement application. The laser sensor is mounted on top of two manual linear stages, in order to align the various components with respect to each other. Initially the illumination beam of the laser sensor is positioned on the lower right corner of the FSM. Since the dimensions of the FSM are known, the laser sensor can then be positioned according to the chosen parameters for y_{FSM} and z_{FSM}. Each axis of the mirror is actuated by two voice coil actuators with moving magnets and static coils. In order to control the current through the coils, two custom made current amplifiers (Type: OPA544T, Texas Instruments Inc., Dallas, USA) with a bandwidth of 10 kHz are used. The angular position of the mirror is measured by an internal optical sensor system. Since the sensing and actuation axes of the FSM are rotated by 45°, a rotation matrix, to transform the actuation signals in the sensing axes, is required. This matrix is implemented in a dSpace platform (Type: DS1202, dSPACE GmbH, Germany) with a sampling rate of 20 kHz.

B. Identification of fast steering mirror

To design a tailored feedback controller for the FSM, the system dynamics of the system must be determined. To identify these dynamics a system analyzer (Type: 3562A, Hewlett-Packard, Palo Alto, USA) is used. The inputs of the analog current controllers and the angular positions of the mirror, serve as the system inputs and outputs, respectively. In Fig. 4, the measured frequency response data (dashed blue) of a single axis of the FSM is shown. Since the structure of the FSM is symmetric the frequency response of both axes are identical (data not shown). The crosstalk magnitude (dash-dotted green) between the axes is over the relevant part of the frequency spectrum 20 dB lower as compared to the single
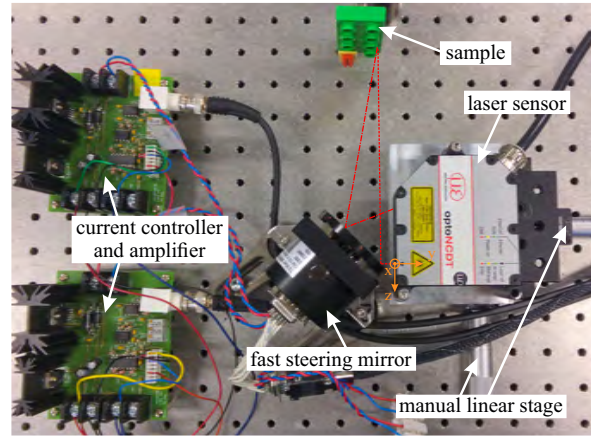

Fig. 3. Experimental setup of the scanning laser triangulation sensor. To align the sensor according to the ray-tracing simulation two manual linear stages are used.

axis transfer function, such that the use of one single-input-single-output (SISO) controller per system axis is justified.
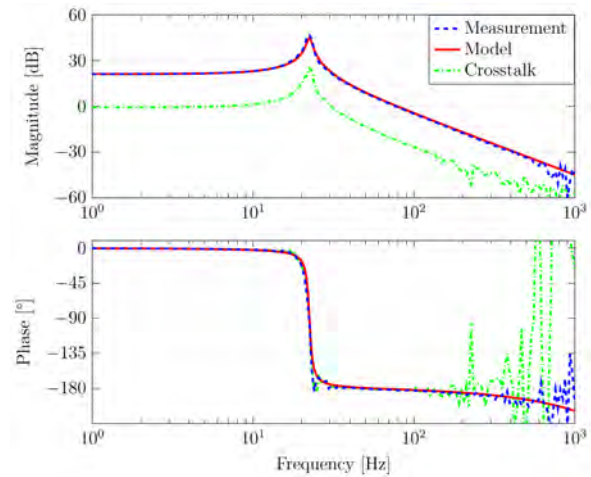

Fig. 4. Measured and modelled frequency response of a single system axis. The natural frequency of the mass-spring-damper system is 22.4 Hz. The measured crosstalk between the two axis is about 20 dB below the single axis response.

The dynamics can be modelled by a mass-spring-damper system with time delay

$$G(s) = \frac{K\omega_s^2}{s^2 + 2\zeta\omega_s + \omega_s^2} e^{-sT_a} \quad \text{(4)}$$

in which K=11.4 is the DC gain, ω_s=140.68 rad/s is the first resonance frequency, ζ=3.21e-2 is the damping ratio and T_a=50 μs is the sampling time of the dSpace platform. The modelled frequency response (solid red) is also depicted in Fig. 4. To select appropriate drive frequencies to scan the area of interest, the maximum frequency of a sinusoidal signal, at which the full scan range of the FSM can still be reached, has to be determined. This frequency is limited by the power

dissipation of the actuator coils (30W), which is reached at a drive frequency of 52 Hz. If a higher drive frequency is selected the achievable actuation range and, consequently, the scan range decreases.

C. Scan trajectories

To scan the area of interest, appropriate scan patterns are required. Lately Lissajous-based scan trajectories, shown in Fig. 5(a), have been utilized for precision scanning systems such as scanning probe microscopy [31]. This trajectory is generated, by driving each system axis with a sinusoidal signal of a single frequency. Since the controller only needs to track the drive frequency of the controlled system axis and reject the drive frequency of the other system axis, a dual tone controller can be utilized [32]. Thereby, the tracking performance of the controller can be improved compared to a classical PID controller [32]. To determine the two drive frequencies of the FSM two conditions need to be considered: (i) the maximum achievable frequency is limited to 52 Hz due to the peak power dissipation of the FSM and (ii) the frequencies need to be well separated, in order to minimize inter-axis crosstalk [32]. According to these conditions the drive frequencies are chosen to 52 Hz and 27 Hz, such that a framerate of 1 frame/s and a spatial resolution of 0.058 (with respect to unity image size) is achieved [33]. The framerate of the scanning system is relatively low as compared to fringe projection techniques, which achieve up to 60 frame/s [34], [35]. However, the scan speed can be further improved by applying a high performance hybrid reluctance force based FSM [26]. If the maximum lateral scan range of 18.5 mm is selected to scan the area of interest, a spatial resolution of 1.07 mm is obtained with the designed trajectory. For lateral scan ranges below 2.2 mm the spatial resolution is determined by the 130 μm laser spot diameter, such that smaller scan ranges do not furhter enhance the resolution.

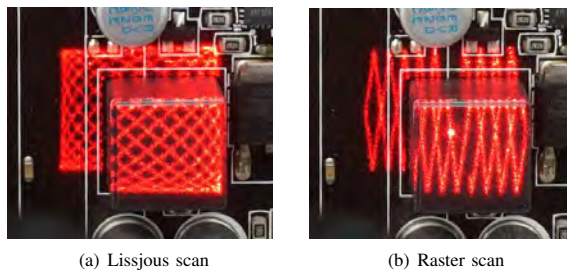(a) Lissjous scan   (b) Raster scan

Fig. 5. Trajectories of (a) a Lissajous scan and (b) a raster scan. The spatial resolution of the Lissajous scan is nonuniform, which can be observed at the edges of the scan area.

Raster scan trajectories, shown in Fig. 5(b), are the most commonly employed scan patterns for atomic force microscopes [31], such that the results measured with this trajectory serve as reference for the Lissajous scans. To generate raster trajectories, one of the system axes is driven with a slow and the other one with a fast triangular signal, such that a uniform spatial resolution and scan speed is achieved [36]. To compare the measurement results of the Lissajous and the raster scan,

the same spatial resolution and framerate is selected. The framerate is determined by the frequency of the slow triangular signal, while the resolution is defined by the frequency ratio between the two triangular signals. Therefore, the frequencies for the slow and fast triangular signal are derived to 2 Hz and 34 Hz, respectively.

In Fig. 6 the simulated imaging process over the measurement time is illustrated. Since the raster scan captures the image line by line, the interesting feature is detected late in the scan process. Due to the multi-resolution property, the feature can already be detected at an earlier stage in the Lissajous case. This can be used to, if necessary, reposition the sample earlier compared to the raster scan.
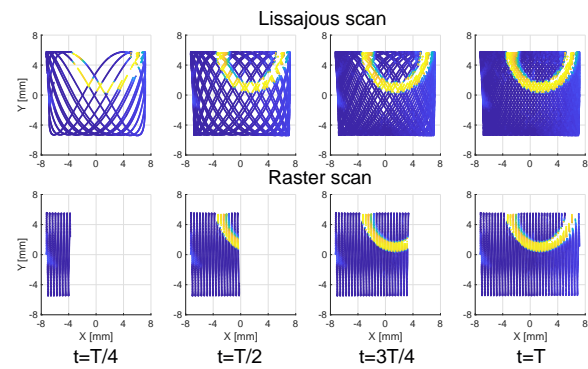
Fig. 6. Simulated image process with the Lissajous and raster trajectory. A preview of the entire scan area is provided and continuously refined by the Lissajous imaging process. Thereby, interesting features can be to detect early in the imaging process. In the raster imaging process the image is acquired line by line.

IV. MOTION CONTROL

To control the system axes of the FSM the cascaded control structure, shown in Fig. 7, is applied to each system axis. The identified system $G(s)$ (see Section III-B) consists of the plant model $P(s)$ and the inner control loop with the analog current controller $C_I(s)$ and the amplifier $A(s)$. Due to the low crosstalk between the two system axes the use of a SISO controller $C_P(s)$ for each system axis is justified.
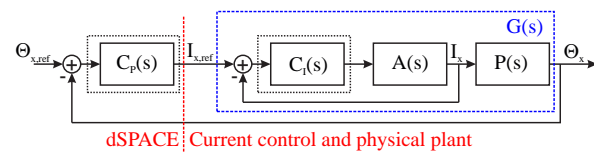
Fig. 7. Control structure applied to each FSM axis. The analog current controller $C_I(s)$ controls the output current of the amplifier $A(s)$. The angular position Θ_x of the mover is controlled by the position controller $C_P(s)$.

For tracking the Lissajous trajectory a dual tone controller [32] is applied to each system axis, as already mentioned in Section III-C. This motion controller shows a high control effort localized at the two frequencies as well as a steep roll-on and roll-of at low and high frequencies, respectively. To design the controller with an H$_\infty$-approach weighting functions for

the sensitivity and the input sensitivity function need to be set in advance. The weighting function for the sensitivity function consists of two inverse notch filters with peaks at the two drive frequencies, such that a good tracking at these two frequencies is achieved [32]. For the weighting function of the input sensitivity function an inverse lowpass and an inverse highpass are combined. The TF reaches its minimum between the driving frequencies, such that a reduced control effort at high and low frequencies is enforced. For the chosen drive frequencies of f_{l1} =27 Hz and f_{l2} =52 Hz the tailored dual tone controller can be derived with an H_∞-approach [32] and results to

$$C_{Dual}(s) = k \cdot \frac{\prod\limits_{i=1}^{2} s + \omega_{az_i}}{s + \omega_{ap_1}} \cdot \frac{\prod\limits_{i=1}^{2} s^2 + 2\zeta_{bz_i}\omega_{bz_i}s + \omega_{bz_i}^2}{\prod\limits_{i=1}^{3} s^2 + 2\zeta_{bp_i}\omega_{bp_i}s + \omega_{bp_i}^2}, \quad (5)$$

with coefficients according to Table I and the gain $k = 179.75$.

TABLE I
COEFFICIENTS OF THE DUAL TONE CONTROLLER

Index	1	2	3
$\omega_{az_{index}}$ [rad/s]	1.26e6	-7.87	-
$\omega_{ap_{index}}$ [rad/s]	4.07e4	-	-
$\zeta_{bz_{index}}$	-2.65e-3	2.55e-2	-
$\omega_{bz_{index}}$ [rad/s]	2.35e2	1.41e2	-
$\zeta_{bp_{index}}$	6.67e-1	1.00e-4	9.96e-5
$\omega_{bp_{index}}$ [rad/s]	1.13e4	3.27e2	1.70e2

Fig. 8 depicts the measured and modelled complementary sensitivity function of the feedback controlled FSM. As can be observed the single axis TF reaches the 0 dB line exactly at the two drive frequencies f_{l1} and f_{l2}. Furthermore, the phase lies at 0° at these frequencies, which means that the reference and output signal are in phase. Due to the positive and negative 20 dB/dec slope at low and high frequencies, the sensor noise feedback is decreased [32]. Compared to a classical PID controller an improved tracking performance can be achieved [32].

To track the raster trajectories with the low-stiffness FSM PID controllers are most commonly used [37]. For the tri-angular drive signals at least the first seven harmonics of the fundamental frequency need to be covered by the system bandwidth [38]. Since the frequency of the fast triangular signal is 34 Hz, a system bandwidth of at least 238 Hz is necessary. The PID alpha tuning method [39] is used to design the PID controller for the required crossover frequency f_c of 240 Hz in the following form 3.6152e+04 To ensure that a robust controller design is accomplished an α-value of three is selected, which leads to the coefficients, for the proportional gain k_p, integral gain k_i and the derivative gain k_d, listed in Table II. The differential action is stopped at ω_t.

In Fig. 9 the measured and modelled complementary sensitivity function of the PID controlled system axis is shown. With the controller a system bandwidth of 422 Hz can be
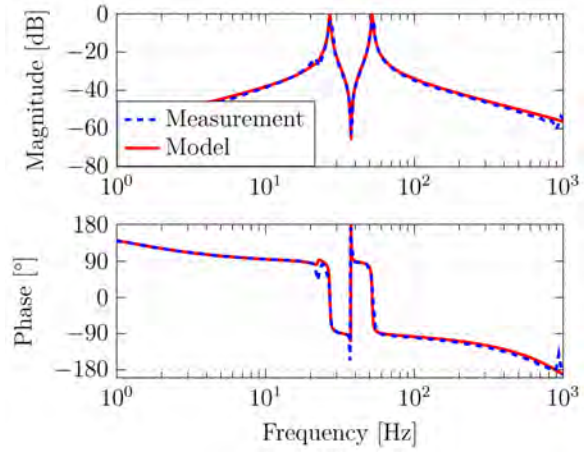

Fig. 8. Measured and modelled complementary sensitivity function of a dual tone controlled system axis. Only at 27 Hz and 52 Hz the magnitude is unity.

TABLE II
COEFFICIENTS OF DESIGNED PID POSITION CONTROLLER.

Parameter	k_p	k_d	k_i	ω_t
Value	2.567	5.8e-3	340.32	4.375e3 rad/s

achieved, which is sufficient to track the desired raster trajectory. Due to the phase margin of 45°, a low gain peaking of 2.8 dB at 155 Hz can be achieved.
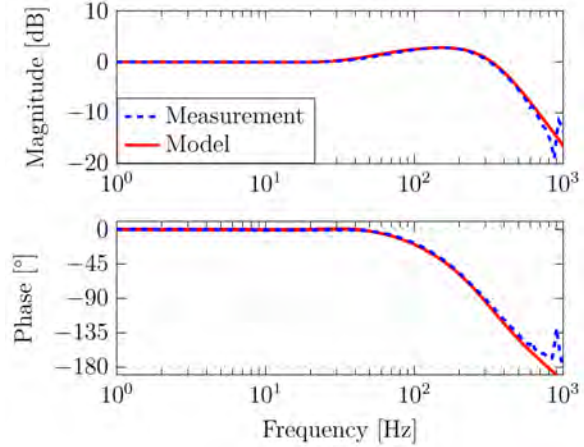

Fig. 9. Measured and modelled complementary sensitivity function of a single PID controlled system axis. The -3 dB system bandwidth is 422 Hz.

V. VALIDATION OF THE MEASUREMENT RESULTS

To validate the measurement results of the Lissajous scans, various samples are measured and the results are compared to the results of the raster scan. Fig. 10 shows the measurement results of a hollow cylinder shaped feature on a duplo brick (Type: Duplo Brick 2 x 4, Lego, Billund, Denmark), which

is positioned at a distance z_s of 130 mm. To make the measurement results comparable, a RANSAC algorithm is applied, which detects the plane area beneath the feature [40]. By subtracting the detected plane from the measurement result, a tilt of the measurement object can be corrected, as described in [16]. As can be observed in the sectional view of Fig. 10, the results of the Lissajous scan show good agreement with the raster scan. In the sectional view along the y-axis some minor artefacts at the edges of the feature are observable in both scans, which are caused by shading effects in the optical path of the laser sensor (Fig. 2). The illumination path is blocked, if the edge of the sample along the x or y-axis is steeper than the angle ϑ or φ, respectively. During the scan along the y-axis also the reflection path may be blocked, which is observable in the sectional view of Fig. 10(d) for the edges at -3 mm and 5 mm. The angle of the reflected beam depends on the effective distance z_s and varies between 71° and 79.1°, such that only edges with a smaller gradient can be measured correctly. Blocking of the optical path is detected by the triangulation sensor and no distance z_{meas} is obtained. Such missing points may be marked in the measured image or interpolated in order to generate the surface profile. In the surface profiles a good agreement between the Lissajous scan and the raster scan is observable. The height of the brick is determined to 4.64 mm with a standard deviation of 225 μm for the raster scan and 4.678 mm with a standard deviation of 183 μm for the Lissajous scan. The height is also measured with a classical mechanical scanning system, consisting of the same laser triangulation sensor and two position controlled linear stages (Type: VT-80 62309160, Physik Instrumente GmbH, Germany), resulting in a measured height of 4.663 mm. The measurements from both scan trajectories show good agreement with the mechanical scanning system, which has a resolution of 1.5 μm.

In summary, the feasibility of a rotational scanning laser sensor is demonstrated and it is shown that Lissajous scans acquire a comparable image quality as raster scans, providing an additional benefit for the scanning application due to the early overview of the entire scan area.

VI. CONCLUSION

In this paper the design, control and the measurement results of a rotational scanning laser sensor for 3D imaging are shown. By determining the system architecture of the scanning system with ray-tracing simulations, the lateral scan range as well as the optical path can be estimated in advance. With the geometrical relations the surface profile can be reconstructed from the measured quantities. If Lissajous-based scan trajectories are used, an overview of the entire scan area is provided already after a fraction of the measurement time. Raster scans are the most commonly employed scan patterns, such that the measurement results of these trajectories serve as reference. To track the Lissajous and raster trajectories tailored dual tone and PID controller, which are based on the identified system dynamics, are designed. The measurement results show, that the calculated surface profile of the Lissajous scan show good agreement with the raster scan and measured

(a) Measurement object

(b) Selected feature

(c) Sectional view x-axis

(d) Sectional view y-axis

(e) Surface profile raster scan
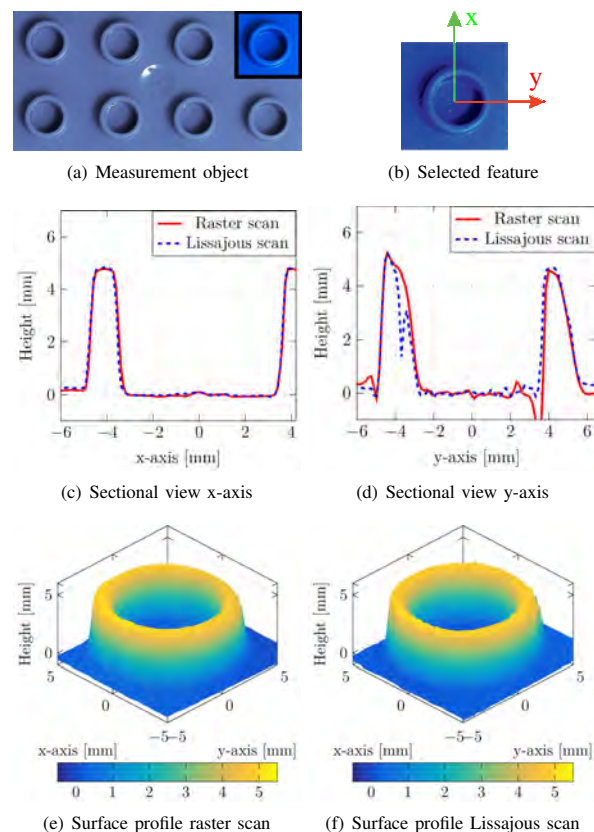

(f) Surface profile Lissajous scan

Fig. 10. Comparison between the raster and Lissajous scan. The artefacts in the Lissajous scan at the edges are caused by multiple reflections. The results of the two scans show good agreement.

height of a classical mechanical scanning system. Therefore, it can be concluded that the rotational scanning motion does not affect on the achievable precision of the sensor system. Current research work is concerned with the performance of the scanning system regarding the achievable resolution and scan speed.

REFERENCES

[1] R. Schmitt and F. Moenning, "Ensure success with inline-metrology," *XVIII IMEKO world congress Metrology for a Sustainable Development*, 2006.
[2] F. Blais, "Review of 20 years of range sensor development," *Journal of Electronic Imaging*, vol. 13, no. 1, 2004.
[3] S. Son, H. Park, and K. H. Lee, "Automated laser scanning system for reverse engineering and inspection," *International Journal of Machine Tools & Manufacture*, vol. 42, pp. 889–897, 2002.

[4] G. Sansoni, M. Trebeschi, and F. Docchio, "State-of-the-art and applications of 3d imaging sensors in industry, cultural heritage, medicine, and criminal investigation," *Sensors*, vol. 9, no. 1, pp. 568–601, 2009.

[5] H. Schwenke, U. Neuschaefer-Rube, T. Pfeifer, and H. Kunzmann, "Optical methods for dimensional metrology in production engineering," *CIRP Annals-Manufacturing Technology*, vol. 51, no. 2, pp. 685–699, 2002.

[6] K. Harding, *Handbook of optical dimensional metrology*. CRC Press, 2013.

[7] C.-S. Liu and S.-H. Jiang, "A novel laser displacement sensor with improved robustness toward geometrical fluctuations of the laser beam," *Measurement Science and Technology*, vol. 24, no. 10, p. 105101, 2013.

[8] S. Hsu, S. Acharya, A. Rafii, and R. New, "Performance of a time-of-flight range camera for intelligent vehicle safety applications," in *Advanced Microsystems for Automotive Applications 2006*. Springer, 2006, pp. 205–219.

[9] S. Zhang, *High-Speed 3D imaging with digital fringe projection techniques*. CRC Press, 2016.

[10] C. P. Keferstein and W. Dutschke, *Fertigungsmesstechnik*. Wiesbaden: Springer Vieweg, 2010.

[11] T. Yoshizawa, *Handbook of optical metrology: principles and applications*. CRC Press, 2015.

[12] B. Chao, L. Yong, F. Jian-guo, G. Xia, L. Lai-peng, and D. Pu, "Calibration of laser beam direction for optical coordinate measuring system," *Measurement*, vol. 73, pp. 191–199, 2015.

[13] P. Giri and S. Kharkovsky, "Detection of surface crack in concrete using measurement technique with laser displacement sensor," *IEEE Transactions on Instrumentation and Measurement*, vol. 65, no. 8, pp. 1951–1953, 2016.

[14] R. Leach, *Optical measurement of surface topography*. Berlin Heidelberg: Springer, 2011, vol. 14.

[15] C. Yu, X. Chen, and J. Xi, "Modeling and calibration of a novel one-mirror galvanometric laser scanner," *Sensors*, vol. 17, no. 1, p. 164, 2017.

[16] J. Schlarp, E. Csencsics, and G. Schitter, "Optical scanning of laser line sensors for 3D imaging," *Applied Optics*, vol. 57, no. 18, pp. 5242–5248, 2018.

[17] K. Noda, N. Binh-Khiem, Y. Takei, T. Takahata, K. Matsumoto, and I. Shimoyama, "Multi-axial confocal distance sensor using varifocal liquid lens," *2013 Transducers & Eurosensors XXVII: The 17th International Conference on Solid-State Sensors, Actuators and Microsystems*, pp. 1499–1502, 2013.

[18] F. J. Brosed, J. J. Aguilar, D. Guilloma, and J. Santolaria, "3d geometrical inspection of complex geometry parts using a novel laser triangulation sensor and a robot," *Sensors*, vol. 11, no. 1, pp. 90–110, 2010.

[19] H. Khali, Y. Savaria, J.-L. Houle, M. Rioux, J.-A. Beraldin, and D. Poussart, "Improvement of sensor accuracy in the case of a variable surface reflectance gradient for active laser range finders," *IEEE Transactions on Instrumentation and Measurement*, vol. 52, no. 6, pp. 1799–1808, 2003.

[20] A. Donges and R. Noll, *Laser measurement technology*. Atlanta: Springer, 2015.

[21] R. H. Webb, "Optics for laser rasters," *Applied optics*, vol. 23, no. 20, pp. 3680–3683, 1984.

[22] S. Xiang, S. Chen, X. Wu, D. Xiao, and X. Zheng, "Study on fast linear scanning for a new laser scanner," *Optics & LASER technology*, vol. 42, no. 1, pp. 42–46, 2010.

[23] A. Wolter, S.-T. Hsu, H. Schenk, and H. K. Lakner, "Applications and requirements for mems scanner mirrors," in *MOEMS and Miniaturized Systems V*, vol. 5719. International Society for Optics and Photonics, 2005, pp. 64–76.

[24] M. Hafez, T. Sidler, R. Salathe, G. Jansen, and J. Compter, "Design, simulations and experimental investigations of a compact single mirror tip/tilt laser scanner," *Mechatronics*, vol. 10, no. 7, pp. 741–760, 2000.

[25] H. F. Mokbel, W. Yuan, L. Q. Ying, C. G. Hua, and A. A. Roshdy, "Research on the mechanical design of two-axis fast steering mirror for optical beam guidance," in *Proceedings of the 1st International Conference on Mechanical Engineering and Material Science*. Atlantis Press, 2012.

[26] E. Csencsics, J. Schlarp, and G. Schitter, "High-performance hybrid-reluctance-force-based tip/tilt system: Design, control, and evaluation," *IEEE/ASME Transactions on Mechatronics*, vol. 23, no. 5, pp. 2494–2502, 2018.

[27] J.-H. Park, H.-S. Lee, J.-H. Lee, S.-N. Yun, Y.-B. Ham, and D.-W. Yun, "Design of a piezoelectric-driven tilt mirror for a fast laser scanner,"

Japanese Journal of Applied Physics, vol. 51, no. 9S2, p. 09MD14, 2012.

[28] G. Schitter, P. J. Thurner, and P. K. Hansma, "Design and input-shaping control of a novel scanner for high-speed atomic force microscopy," *Mechatronics*, vol. 18, no. 5-6, pp. 282–288, 2008.

[29] F. Marinello, E. Savio, P. Bariani, and S. Carmignato, "Coordinate metrology using scanning probe microscopes," *Measurement Science and Technology*, vol. 20, no. 8, p. 084002, 2009.

[30] B.-F. Ju, W.-L. Zhu, S. Yang, and K. Yang, "Scanning tunneling microscopy-based in situ measurement of fast tool servo-assisted diamond turning micro-structures," *Measurement Science and Technology*, vol. 25, no. 5, p. 055004, 2014.

[31] T. Tuma, J. Lygeros, V. Kartik, A. Sebastian, and A. Pantazi, "High-speed multiresolution scanning probe microscopy based on lissajous scan trajectories," *Nanotechnology*, vol. 23, no. 18, p. 185501, 2012.

[32] E. Csencsics and G. Schitter, "System design and control of a resonant fast steering mirror for lissajous-based scanning," *IEEE Transactions on Mechatronics*, vol. 22, no. 5, pp. 1963–1972, 2017.

[33] T. Tuma, J. Lygeros, A. Sebastian, and A. Pantazi, "Optimal scan trajectories for high-speed scanning probe microscopy," in *American Control Conference (ACC), 2012*. IEEE, 2012, pp. 3791–3796.

[34] Q. Guo, Y. Ruan, J. Xi, L. Song, X. Zhu, Y. Yu, and J. Tong, "3d shape measurement of moving object with fft-based spatial matching," *Optics & Laser Technology*, vol. 100, pp. 325–331, 2018.

[35] S. Zhang, "Recent progresses on real-time 3d shape measurement using digital fringe projection techniques," *Optics and lasers in engineering*, vol. 48, no. 2, pp. 149–158, 2010.

[36] L. R. Hedding and R. A. Lewis, "Fast steering mirror design and performance for stabilization and single-axis scanning," in *Orlando'90, 16-20 April*. International Society for Optics and Photonics, 1990, pp. 14–24.

[37] D. J. Kluk, M. T. Boulet, and D. L. Trumper, "A high-bandwidth, high-precision, two-axis steering mirror with moving iron actuator," *Mechatronics*, vol. 22, no. 3, pp. 257–270, 2012.

[38] J. A. Fleming and G. A. Wills, "Optimal periodic trajectories for band-limited systems," *IEEE Transactions on Control Systems Technology*, vol. 17, no. 3, pp. 552–562, 2009.

[39] E. Csencsics and G. Schitter, "Parametric PID controller tuning for a fast steering mirror," in *1st IEEE Conference on Control Technology and Applications*, Kohala Coast, Hawaii, USA, 2017.

[40] F. Tarsha-Kurdi, T. Landes, and P. Grussenmeyer, "Hough-transform and extended ransac algorithms for automatic detection of 3d building roof planes from lidar data," in *ISPRS Workshop on Laser Scanning 2007 and SilviLaser 2007*, vol. 36, 2007, pp. 407–412.